NOTE • OPEN ACCESS

Technical note: development of a simulation framework, enabling the investigation of locally tuned single energy proton radiography

Biomedical Physics & Engineering Express

NOTE

Technical note: development of a simulation framework, enabling the investigation of locally tuned single energy proton radiography

Måns Lundberg[1,2,*], **Arturs Meijers**[2], **Kevin Souris**[3], **Sylvain Deffet**[3], **Damien C Weber**[2,4,5], **Antony Lomax**[2,6] **and Antje Knopf**[1]

[1] Institute for Medical Engineering and Medical Informatics, School of Life Science FHNW, Muttenz, Switzerland
[2] Center for Proton Therapy, Paul Scherrer Institute, Villigen, Switzerland
[3] Ion Beam Applications SA, Louvain-La-Neuve, Belgium
[4] Department of Radiation Oncology, University Hospital of Zürich, Zürich, Switzerland
[5] Department of Radiation Oncology, Inselspital, Bern University Hospital, University of Bern, Bern, Switzerland
[6] Department of Physics, ETH Zurich, Zurich, Switzerland
[*] Author to whom any correspondence should be addressed.

E-mail: mans.lundberg@fhnw.ch

Keywords: proton radiography, quality control, proton therapy

OPEN ACCESS

RECEIVED
27 September 2023

REVISED
29 November 2023

ACCEPTED FOR PUBLICATION
19 January 2024

PUBLISHED
7 February 2024

Abstract

Range uncertainties remain a limitation for the confined dose distribution that proton therapy can offer. The uncertainty stems from the ambiguity when translating CT Hounsfield Units (HU) into proton stopping powers. Proton Radiography (PR) can be used to verify the proton range. Specifically, PR can be used as a quality-control tool for CBCT-based synthetic CTs. An essential part of the work illustrating the potential of PR has been conducted using multi-layer ionization chamber (MLIC) detectors and mono-energetic PR. Due to the dimensions of commercially available MLICs, clinical adoption is cumbersome. Here, we present a simulation framework exploring locally-tuned single energy (LTSE) proton radiography and corresponding potential compact PR detector designs. Based on a planning CT data set, the presented framework models the water equivalent thickness. Subsequently, it analyses the proton energies required to pass through the geometry within a defined ROI. In the final step, an LTSE PR is simulated using the MCsquare Monte Carlo code. In an anatomical head phantom, we illustrate that LTSE PR allows for a significantly shorter longitudinal dimension of MLICs. We compared PR simulations for two exemplary 30×30 mm^2 proton fields passing the phantom at a 90° angle at an anterior and a posterior location in an iso-centric setup. The longitudinal distance over which all spots per field range out is significantly reduced for LTSE PR compared to mono-energetic PR. In addition, we illustrate the difference in shape of integral depth dose (IDD) when using constrained PR energies. Finally, we demonstrate the accordance of simulated and experimentally acquired IDDs for an LTSE PR acquisition. As the next steps, the framework will be used to investigate the sensitivity of LTSE PR to various sources of errors. Furthermore, we will use the framework to systematically explore the dimensions of an optimized MLIC design for daily clinical use.

1. Introduction

Proton therapy (PT) has the ability to deliver more confined dose distributions compared to conventional radiotherapy using photons. Conformal high-dose regions are used to treat targets close to organs at risk. However, uncertainties can compromise the dose-sparing potential of protons, resulting in unwanted irradiation of healthy tissue. Causes of uncertainties are inaccuracies during patient positioning, organ motion, anatomy changes and range uncertainty, among others. Accurate knowledge of the patient's anatomy and the expected proton range just prior to irradiation is therefore of great value for an accurate proton dose delivery.

Most proton therapy machines nowadays are equipped with CBCT, allowing for imaging in treatment position, just prior to irradiation. CBCT

provides day-specific information about the patient's anatomy. However, CBCTs experience various imaging artifacts preventing their direct use for proton dose calculation (Giacometti *et al* 2020, Thummerer *et al* 2020). The translation of CBCTs into synthetic CTs (Thummerer *et al* 2021) as well as the inherent ambiguity of translating HUs into relative stopping powers (RSP) (Yang *et al* 2012), required for proton dose calculations, results in range uncertainties.

Proton radiography (PR) has shown to be a valuable asset to verify the proton range and consequently mitigate range uncertainties (Schneider *et al* 1995, Mumot *et al* 2010, Farace *et al* 2016, Meijers *et al* 2020, Meijers *et al* 2021). Several approaches have been explored to mitigate the range uncertainty in proton therapy such as proton CT to bypass the ambiguous CT to RSP conversion (Collins-Fekete *et al* 2020, DeJongh *et al* 2021, Dickmann *et al* 2021) and by creating a patient-specific CT to RSP calibration (Krah *et al* 2019). Image quality in proton imaging is compromised by multi-Coulomb scatter, which has to be accounted for either by computer models (van der Heyden *et al* 2021) or by tracking the protons' trajectory before and after the patient, which can complicate the hardware setup.

PR has also been used to verify patient positioning (Hammi *et al* 2017, Hammi *et al* 2018) and recently it has specifically demonstrated its potential as a quality control tool of CBCT-based synthetic CTs in an adaptive PT workflow (Seller Oria *et al* 2021, Thummerer *et al* 2021, Thummerer *et al* 2022).

Adaptive PT in particular relies on information about the patient in treatment position just prior to dose delivery, as it aims to adjust the dose distribution to the up-to-date anatomy (Nenoff *et al* 2021, Paganetti *et al* 2021, Bobić *et al* 2023).

An essential part of the research related to PR has so far been conducted with the commercially available Multi-Layer Ionisation Chamber (MLIC) Giraffe (IBA Dosimetry, Schwarzenbruck, DE). Traditionally, PR employs mono-energetic proton beams of high energy, enabling the protons to traverse larger Water Equivalent Thickness (WET) areas. However, the approach results in high residual proton energies after the patient, particularly in low WET areas, necessitating a substantial longitudinal dimension of the MLIC.

The commercially available Giraffe MLIC detector has a dimension of 439 $\times$ 17 $\times$ 19.5 cm and offers a maximum measurable range of 360 mm. It consists of 180 air-vented parallel plane ionization chambers with a 2 mm gap, a longitudinal accuracy of $\pm$ 0.5 mm and electrodes of 12 cm in diameter, according to the manufacturer. The handling of the Giraffe MLIC can be cumbersome, and hence, it is difficult to integrate PR into daily clinical workflows.

In this work, we present a PR simulation framework to explore MLIC designs that would be better suited for daily clinical use, aiming at verifying the HU estimated in CBCT-based synthetic CTs by measuring and comparing the residual range between in-vivo and in-silico acquired depth dose curves. The framework is based on the concept of locally tuned single energy (LTSE) PR.

Contrary to flat panel PR where multiple acquisitions of mono-energetic protons are used to image the entire geometry, the LTSE PR employs a single irradiation field with proton energies optimized per spot. Spot-by-spot energy investigation has been performed with flat-panel detector (Seller Oria *et al* 2023), but by eliminating spots that would have otherwise been absorbed within the patient to reduce the imaging dose.

To our knowledge, this is the first study presenting a framework for LTSE PR simulations. Within the framework, we introduce an energy selection algorithm that chooses proton spot energies per spot, depending on the WET in a region of interest (ROI). The framework then calculates LTSE PR. We show the accordance of simulated and experimentally acquired LTSE PR and illustrate the potential to significantly shorten the longitudinal MLIC dimensions when using LTSE PR instead of mono-energetic PR.

2. Material and method

2.1. Proton radiography simulation framework

The LTSE PR simulation framework presented here comprises the following parts: (i) generation of a WET map based on a CT data set, (ii) creation of an energy map by translating the WET map into proton energy, (iii) choice of a ROI for PR imaging, and selection of an energy per spot, sufficient to just pass the geometry within the ROI, and (iv) the LTSE PR simulation. An overview of the framework is given in figure 1.

In part (i) of the framework, depending on the chosen imaging angle, a WET map is generated based on a given CT using OpenREGGUI (https://openreggui.org/). The WET is generated by first translating HU from the CT into mass densities according to a user-defined lookup table. Mass densities are then translated into stopping power ratios according to the conversion scheme used in RayStation version 4.7. Finally, a 2D WET map is created considering the physical dimensions of the various materials in the beam path and their stopping power ratios.

In part (ii) an energy map is created by calculating proton energies, sufficient to just pass the geometry. Each 1×1 mm^2 pixel of the WET map is translated into a proton energy using PSTAR Continuous Slowing Down Approximation (CSDA) in water (https://physics.nist.gov/PhysRefData/Star/Text/PSTAR.html). To ensure the penetration of the anatomy, the closest integer energy that exceeded WET plus an energy equivalent range in the order of 3 cm in water is chosen.

The choice of additional energy creates a trade-off situation; a lower value enables a smaller longitudinal shape of the MLIC at the cost of the increased likelihood of the BP being absorbed in the patient.

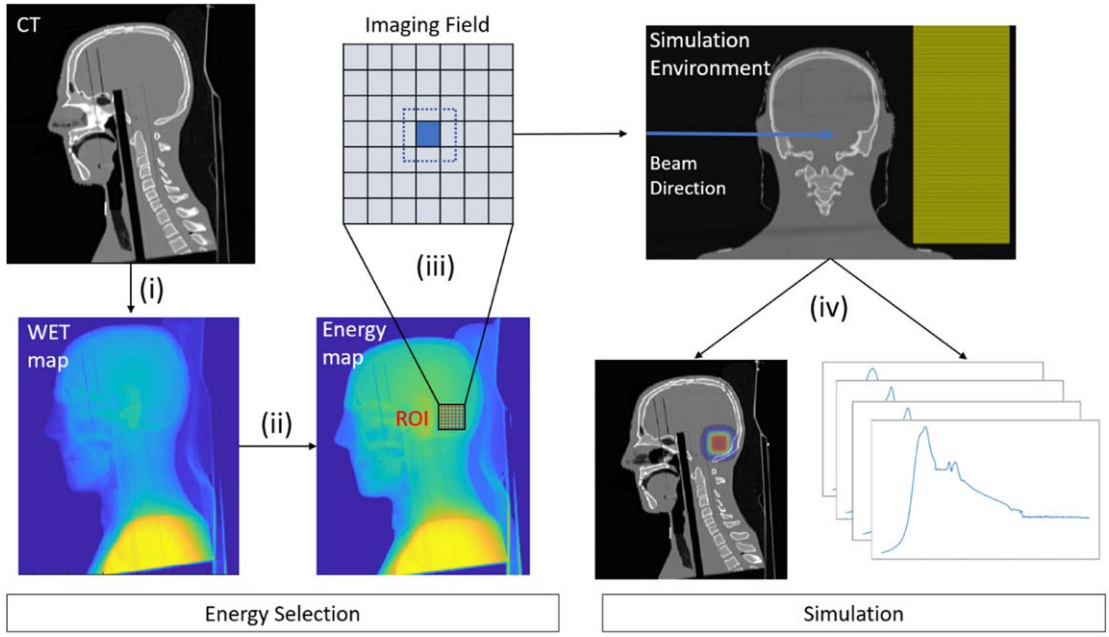

Figure 1. Schematic illustration of the framework: (i) creation of a WET map based on a given CT image, (ii) translation of the WET map into a proton energy map, (iii) definition of a ROI and a spot spacing. For each spot, an energy optimization is performed, ensuring that the protons will have enough energy to just pass through the anatomy. Lastly, a LTSE PR simulation is performed. In the simulation environment shown in the top right, the proton beams per spot position enters from left, pass through the patient, and deposit their remaining energy in the water block that mimics the MLIC. The simulation output (iv) is a 3D dose distribution, from which IDD curves are derived.

Conversely, a higher value would necessitate a larger MLIC longitudinal size but would mitigate potential adverse effects on the patient. Further explanation can be found in the discussion.

In part (iii) of the framework, a ROI can be chosen for which a PR will be simulated via a user interface. The user has the flexibility to create a ROI at any position and of any size on the energy map and/or define parameters for a box placed around the isocenter, with the isocenter itself being determined by the loaded treatment plan. For the ROI, the spot spacing for the PR simulation can be set to any integer value limited by the pixel size of the energy map. The number of spots for the PR simulation is defined depending on the ROI and the spot spacing.

In part (iv) of the framework, the energy per spot for the LTSE PR simulation is optimized. Various contributions such as lateral inhomogeneities, multiple Coulomb scattering and range straggling, can dilute the Bragg peak per spot position. The energy selection needs to account for these ambiguities in order to ensure the spot reaches the detector to achieve an optimal PR signal. To account for lateral inhomogeneities per spot position, the 85th percentile energies averaged over an 11×11 mm^2 region around the spot center are taken as the spot energy. Energies between 40 to 70 MeV are automatically adjusted to 70 MeV due to the minimum energy limit of the beam delivery system. Spot positions, where the energy selection algorithm finds energies lower than 40 MeV are neglected. Spot energies are written into a DICOM ion plan, which can be used afterwards either for the delivery at a proton machine to measure the PR or be used for a simulation of PR as described in the following section.

In the final part (v) of the framework, the LTSE PR is simulated using MCsquare (Souris *et al* 2016) within OpenREGGUI. MCsquare is a Monte Carlo simulation environment for proton therapy that is highly versatile and fast, designed for use on massively parallel CPU architectures. Using the class-II condensed history algorithm, MCsquare is able to efficiently and precisely simulate the transport of heavy charged particles in voxelized geometries. MCsquare simulations in OpenREGGUI were performed using 10^6 protons per spot. A water equivalent block needs to be included in the CT at the distal end of the geometry; mimicking the MLIC and scoring the distal energy deposition of the PR field (see figure 1).

The output of the simulations is a dose distribution volume for each spot, with a $1 \times 1 \times 1$ mm^3 voxel size. Integral depth dose curves (IDD) can be created by integrating the dose distribution along the beam axis.

2.2. Proof of concept

Mono-energetic and LTSE PR for an anterior and a posterior ROI through a head phantom were simulated using the above-introduced framework. Accordingly, LTSE PR was experimentally acquired. The beam model used for the MC simulations matched the energy spread and nominal energy of the experimental beam within clinically acceptable tolerances: peak

Figure 2. On the left: Position of the two ROI in the used head phantom. On the right: Experimental setup: the MLIC is positioned along the isocenter beam axis, on the distal end of the head phantom. The head phantom is placed AP on an immobilization pillow at the top of the couch. The gantry is positioned at 90°.

width discrepancy and range accuracy of less than 1 mm in water. The experimental setup is illustrated in figure 2.

2.2.1. Testing environment

A head phantom, consisting of several tissue-equivalent plates, sliced from left to right was used (adaptive head and neck phantom, MediTron). A CT scan of the phantom in head-first supine position was acquired. Based on the CT, two PR plans were created, choosing a 90° gantry angle so that the proton beams would enter the phantom perpendicularly to the plate slicing. Two $30 \times 30\,mm^2$ ROI were chosen in accordance with the size of the field of view (FOV) of the used MLIC detector to ensure full detection of all PR spots. ROI 1 was positioned posteriorly so that PR spots would mainly pass through a homogeneous geometry; ROI 2 was positioned anteriorly so that PR spots would encounter some inhomogeneities in the area of nasal cavities. A spot separation of 5 mm was chosen, resulting in $7 \times 7 = 49$ spots per PR field.

2.2.2. Comparison mono-energetic and LTSE PR simulation

For both ROIs mono-energetic and LTSE PR were simulated. LTSE PRs were simulated using the introduced framework above. The simulation environment for the mono-energetic PR was identical, except that each spot energy was set to 210 MeV.

2.2.3. Comparison of simulated and experimentally acquired IDDs for a LTSE PR approach

Experimental LTSE PRs for both ROI were acquired at Gantry 3 at the center for proton therapy at Paul Scherrer Institute, Villigen Switzerland, using the commercially available Multi-Layer Ionisation Chamber (MLIC) Giraffe (IBA Dosimetry, Schwarzenbruck, DE). Measurements were performed in movie-mode for 40 s with a 10 ms sampling time. Before acquiring the PR fields a gain calibration as recommended by the vendor of the MLIC was performed. Afterwards, the head phantom was positioned supine on an immobilization pillow on the couch using kV x-ray. The alignment to the plan isocenter was verified with CBCT. The gantry was positioned at 90° and the MLIC was placed on the distal side of the phantom on a trolley, as illustrated in figure 2. MLIC was positioned vertically and longitudinally based on the in-room lasers.

For the PR acquisition, a time delay had to be introduced after each spot delivery in order to separate the signal per spot position in the MLIC. Each field of 49 spots consisted of 49 unique energies. The maximum energy change per spot was 1.5 and 3 MeV for ROI 1 and 2 accordingly.

The MLIC Output per PR field is a single file showing the counts per each chamber over time, which is interpreted in OpenREGGUI to determine the measured dose and subsequently create the IDD's.

Least square method was used to align the simulated and measured IDD's, with the resulting best-fit shift being considered as the residual range error. In order to focus on the alignment of the Bragg peak, a weighted least square method was used. Signal to the power of 3 was used as a weighting factor.

3. Results

3.1. Comparison of mono-energetic and LTSE PR simulation

Figure 3 shows 49 IDD's per ROI once simulated in a mono-energetic approach using 210 MeV for each spot position and once using a LTSE approach with an energy selection as described in the framework above.

In the mono-energetic approach, proton spots have a high remaining energy after passing the geometry resulting in a signal detected up to approximately 160 mm for ROI 1 and up to 230 mm for ROI 2. Energy optimization results in significantly lower signal ranges for the LTSE approach (up to approximately 45 mm for RIO 1 and 100 mm for ROI 2). Furthermore, the longitudinal distance over which all spots per PR field range out is significantly reduced in the LTSE approach. For ROI 1 the longitudinal range-

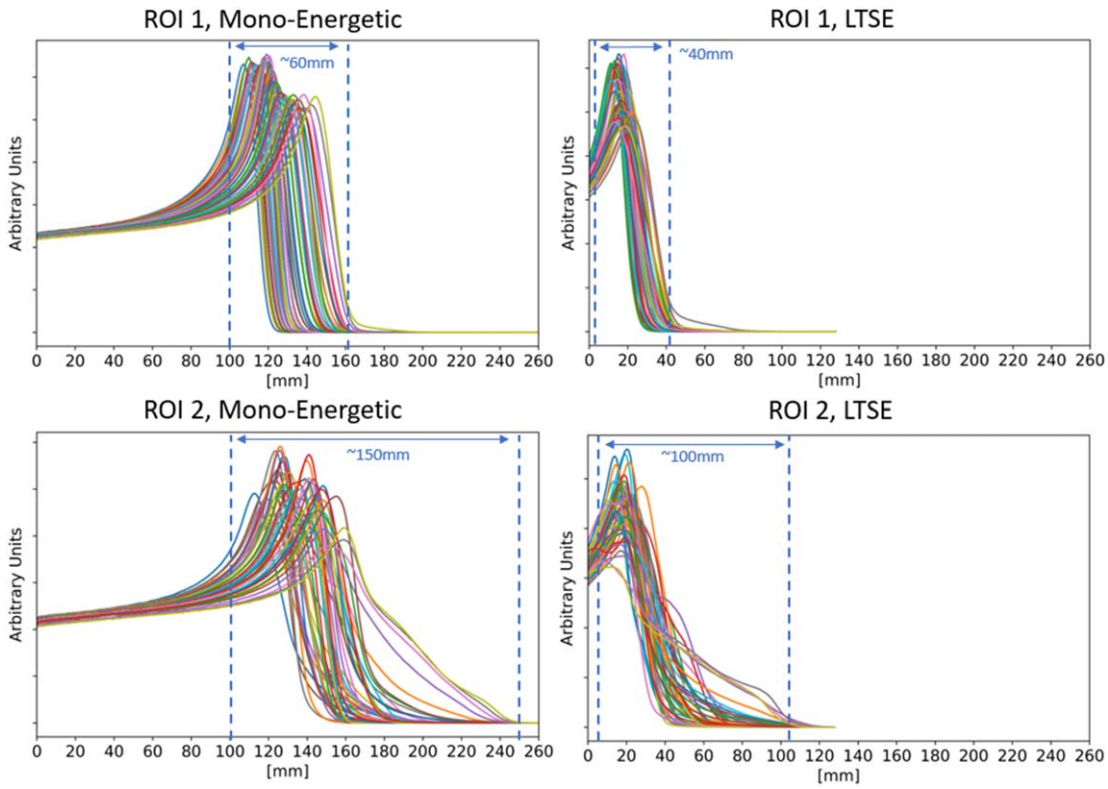

Figure 3. 49 IDD's for ROI 1 (top) and ROI 2 (bottom), once simulated in a mono-energetic approach (left) using 210 MeV for each spot position and once using a LTSE approach (right). Blue dotted lines indicate the longitudinal distance over which all spots per ROI approximately range out.

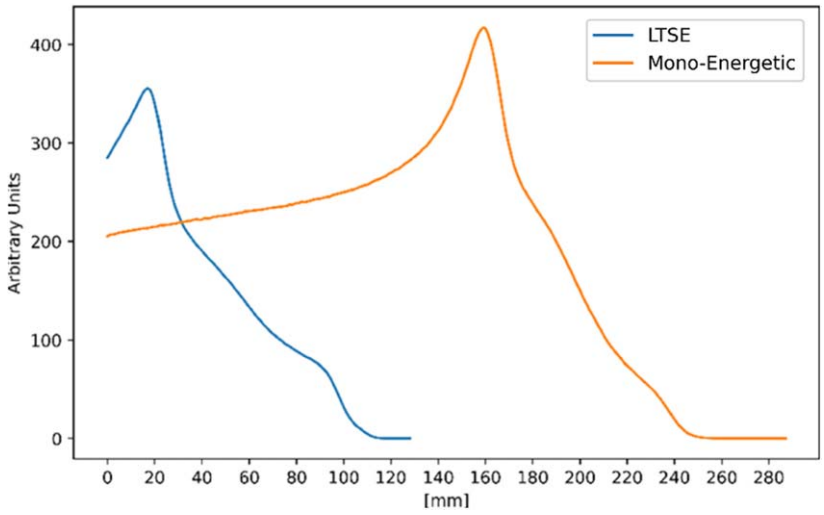

Figure 4. Exemplary IDDs at the same position within ROI 2, simulated once with 210 MeV in the mono-energetic approach and once for with 141 MeV, as determined by the energy selection algorithm of the LTSE approach.

out distance could be reduced from approximately 60 mm to approximately 40 mm and for ROI 2 from 150 mm to 100 mm. The larger range-out distance for ROI 2 compared to ROI 1 can be explained by the higher geometry inhomogeneities present for ROI 2.

Figure 4 shows two exemplary IDDs at the same position within ROI 2, simulated once with 210 MeV in the mono-energetic approach and once for 141 MeV, as determined by the energy selection algorithm of the LTSE approach. One can see slight differences in the shape of the distal fall-off, resulting from the different impact of range straggling on proton beams with higher and lower energy. The variation in Bragg peak distortion occurs due to the fact that lower energy spots have a larger spot size (sigma at 210 MeV is 3.26 mm versus 4.15 mm at 141 MeV). As a result

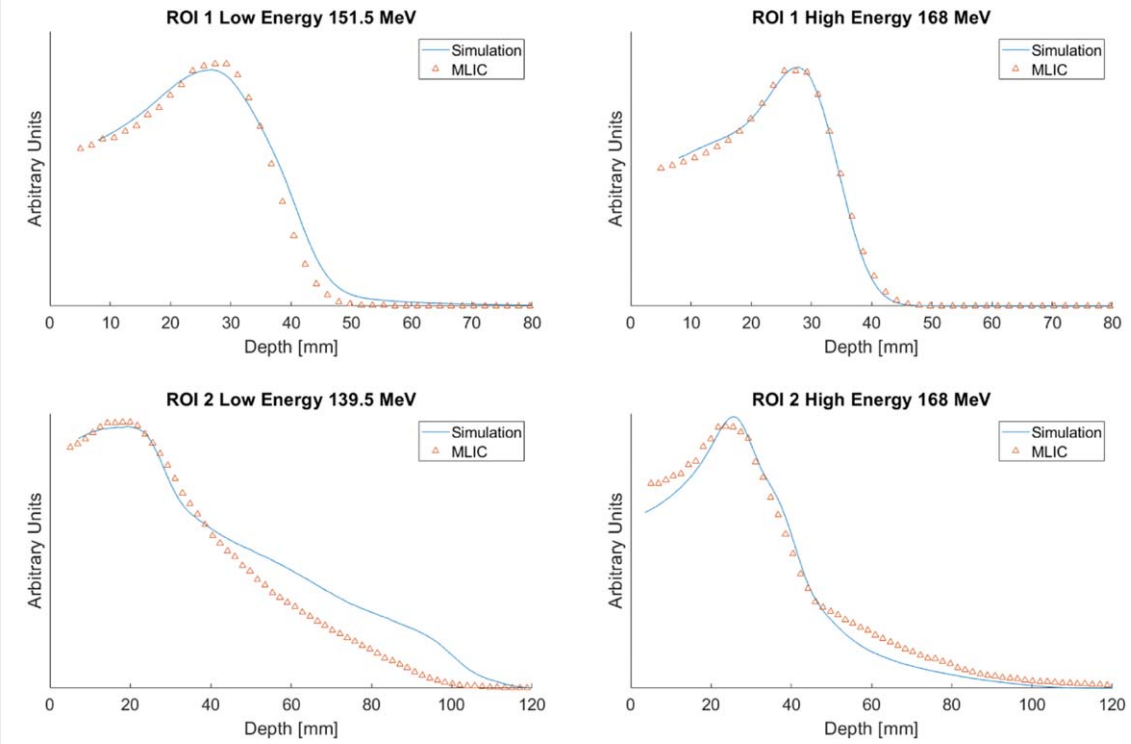

Figure 5. Comparison of exemplary measured and simulated IDDs. The highest (right) and lowest (left) energy spots for ROI 1 (top) and ROI 2 (bottom) were chosen to illustrate shape accordance between measured and simulated IDDs in a LTSE PR approach.

lower energy spots will sample a larger area laterally. When passing through highly heterogeneous environments, such as nasal cavities, this will result in different energy mixing.

3.2. Shape comparison of simulated and experimentally acquired IDDs for a LTSE PR approach

In figure 5, simulated and measured IDDs for the lowest and highest energy per ROI in the LTSE approach are compared to demonstrate shape accordance. A median filter was applied with a 3 channel kernel to the experimentally acquired IDDs to lower noise. Filtering is required since measurements are performed with low MU spots to minimize imaging dose. For comparison, the MU per spot used in PR imaging is approximately 3000 lower than what is used in recurrent machine QA procedures. Range deviations as well as differences in absolute values between simulated and measured IDDs were determined using the least square method within the detector volume. The simulated IDDs were shifted and normalized accordingly to best overlay with the experimentally acquired IDDs. The applied shifts along the depth axis correct for residual range errors. The shifts did not exceed the range uncertainty margin defined as 2.4% + 1.2 mm. Such magnitude of residual range errors is in line with broadly accepted range uncertainty margin recipes (Paganetti 2012). Residual range errors are present due to sources of range uncertainty (Paganetti 2012) and uncertainties linked to the range probing technique, such as: spot position accuracy, energy reproducibility, residual setup error of the phantom, MLIC calibration accuracy and resolution, dose discretization in the simulations (Meijers *et al* 2021), among others. Furthermore, measurements are performed on plastic head phantom, while CT calibration curves used in the simulations are tuned for animal-like tissues.

For ROI 1 IDDs show good agreement in terms of shape, specifically for the distal fall-off. For ROI 2 slight deviations can be observed, attributed to the higher inhomogeneity of the passed through geometry and the resulting higher energy straggling experienced per spot. As a result, spots in ROI 2 are more sensitive to residual positioning errors of the phantom.

4. Discussion

In the current implementation of the energy selection, a water equivalent range offset in the order of 3 cm is added when creating the energy map to ensure that protons pass through the geometry and range out in the MLIC detector. A smaller offset would make the LTSE PR approach more sensitive to patient positioning error where even a small WET increase could cause the protons to range out in the anatomy instead of the detector and increase the dose delivered to the patient, as partly seen in the left bottom frame of figure 5. However, increasing the energy offset results in larger residual energies of the protons, requiring a larger

longitudinal dimension of the MLIC detector to capture their full ranging out.

In a clinical environment, ROI2 would not be an ideal PR location due to the lateral inhomogeneities. Choosing a homogeneous ROI, an additional energy equivalent range in the order of 3 cm seems suitable. The exact nominal value for the offset, assuring robustness as well as a minimal longitudinal dimension of the MLIC detector, is subject to further investigation.

With an LTSE PR approach, the imaging dose to the patient will increase since part of the proximal rise of the Bragg Peak will already start in the patient. This increase can be up to 3.5 times (peak to plateau ratio) compared to a mono-energetic PR approach. Nevertheless, such imaging dose could be accounted for in the treatment planning process. The imaging dose optimization problem is subject to further investigations using the proposed simulation framework.

Lateral inhomogeneities greatly affect the proton trajectories, specifically for low-energy beams. To ensure that most of the protons per spot pass through the geometry, the energy selection process currently chooses a spot energy corresponding to the 85th percentile of an 11×11 mm^2 averaging area around the spot center. Whether this is an optimal choice for averaging and optimizing the energy per spot needs further investigation using the proposed framework.

Figure 4 illustrates that slight deviations in IDD shape can occur when using high or low energies for PR, due to a different impact of range straggling on high- and low-energy proton beams (Newhauser *et al* 2015). Differences in the IDD shape pose questions on the methodology to compare IDDs. Currently, the least square method is used for IDD alignment. Other methods might be more appropriate when looking at IDDs of more complex shapes and limited longitudinal extent.

Ramping of beam energies in the cyclotron costs time. To optimize experimental LTSE PR acquisition time, the current implementation allows for a batching of the resulting energies, minimizing the number of different energies requested per ROI. For that, the resulting energy per spot can be rounded up to the closest value of a user-defined energy quantization. The practicability and an optimal batch size have to be further investigated experimentally.

Figure 5 shows a comparison of simulated and experimentally acquired IDD. Simulated IDDs were shown to be representative and plausible in shape when compared to the experimentally acquired IDD data set. Deviations might result from differences in the considered integration area for the simulation and the experiment. For the experiment, the signal is integrated over the circular area of the signal electrode with a diameter of 12 cm. For the simulation, the signal is integrated over the entire squared dimension of the water block (50×30 cm, also see figure 1) that mimics the detector. Generally, the framework provides the possibility to generate IDD integrating over any user-defined sensitive volume of the detector and taking into account the spot position with respect to the center of the sensitive volume. This provides the capability to investigate an optimal sensitive volume choice for the new MLIC detector in future work.

Deviations in the shape between measured and experimentally acquired IDDs might further result from the fact that the head phantom materials are not perfectly represented by the used CT calibration curve. CT calibration curves used in proton therapy are optimized for human-like tissues, while the phantom is made of tissue substitute materials, which do not necessarily mimic the elemental composition of human-like tissues. This might result in inaccuracies in scattering properties within the simulation, leading to deviations as seen for ROI 2 in figure 5, where the protons travel through highly inhomogeneous regions of the phantom.

Furthermore, in highly heterogeneous environments, such as nasal cavities of the head phantom (ROI2), small deviations in the position of the phantom with regards to the isocenter will result in different energy mixing, therefore, affecting the shape of the curve. Considering the accuracy of the positioning system and spot position accuracy of the beam delivery system, positioning uncertainty on the order of 1 mm can be expected for the experimental setting.

Figure 3 illustrates the potential of a LTSE PR approach to decrease the longitudinal dimension of MLIC detectors. Due to the optimal energy selection, the residual range of the protons is smaller as well as the distance over which all protons per ROI range out.

In addition, it remains an open question whether it is necessary to detect the full distal range-out for meaningful range verification via LTSE PR. This could allow further scope to decrease the longitudinal dimension of MLIC detectors.

The presented framework enables the simulation of LTSE PR. To our knowledge, this permits for the first time to systematically investigate the potential and limitations of LTSE PR. In follow-up studies, we will use the presented framework to systematically explore the potential to optimize MLIC detector designs for daily clinical use, based on a LTSE PR approach.

Data availability statement

The data that support the findings of this study are openly available at the following URL/DOI: https://github.com/lundberg91/RawData/tree/e84048dc93206e94b16c2562de0efb62de61c60b/Technical%20note%20Development%20of%20a%20simulation%20framework%2C%20enabling%20the%20investigation%20of%20locally%20tuned%20single%20energy%20proton%20radiography.

ORCID iDs

Måns Lundberg https://orcid.org/0009-0009-7738-8967

References

Bobić M *et al* 2023 Large anatomical changes in head-and-neck cancers - a dosimetric comparison of online and offline adaptive proton therapy *Clin. Transl. Radiat. Oncol.* **40** 100625

Collins-Fekete C A *et al* 2020 Statistical limitations in proton imaging *Phys. Med. Biol.* **65** 085011

DeJongh E A *et al* 2021 Technical note: a fast and monolithic prototype clinical proton radiography system optimized for pencil beam scanning *Med. Phys.* **48** 1356–64

Dickmann J *et al* 2021 Proof of concept image artifact reduction by energy-modulated proton computed tomography (EMpCT) *Phys Med.* **81** 237–44

Farace P *et al* 2016 Pencil beam proton radiography using a multilayer ionization chamber *Phys. Med. Biol.* **61** 4078–87

Giacometti V *et al* 2020 A review of dose calculation approaches with cone beam CT in photon and proton therapy *Phys Med.* **76** 243–76

Hammi A *et al* 2017 Positioning of head and neck patients for proton therapy using proton range probes: a proof of concept study *Phys. Med. Biol.* **63** 015025

Hammi A *et al* 2018 Patient positioning verification for proton therapy using proton radiography *Phys. Med. Biol.* **63** 245009

Krah N *et al* 2019 Regularised patient-specific stopping power calibration for proton therapy planning based on proton radiographic images *Phys. Med. Biol.* **64** 065008

Meijers A *et al* 2020 Validation of the proton range accuracy and optimization of CT calibration curves utilizing range probing *Phys. Med. Biol.* **65** 03NT02

Meijers A *et al* 2021 Technical note: first report on an *in vivo* range probing quality control procedure for scanned proton beam therapy in head and neck cancer patients *Med. Phys.* **48** 1372–80

Mumot M *et al* 2010 Proton range verification using a range probe: definition of concept and initial analysis *Phys. Med. Biol.* **55** 4771–82

Nenoff L *et al* 2021 Experimental validation of daily adaptive proton therapy *Phys. Med. Biol.* **66** 205010

Newhauser W D *et al* 2015 The physics of proton therapy *Phys. Med. Biol.* **60** R155–209

Paganetti H 2012 Range uncertainties in proton therapy and the role of Monte Carlo simulations *Phys. Med. Biol.* **57** R99–117

Paganetti H *et al* 2021 Adaptive proton therapy *Phys. Med. Biol.* **66** 22TR01

Schneider U *et al* 1995 Proton radiography as a tool for quality control in proton therapy *Med. Phys.* **22** 353–63

Seller Oria C *et al* 2021 Range probing as a quality control tool for CBCT-based synthetic CTs: *In vivo* application for head and neck cancer patients *Med. Phys.* **48** 4498–505

Seller Oria C *et al* 2023 Technical note: flat panel proton radiography with a patient specific imaging field for accurate WEPL assessment *Med. Phys.* **50** 1756–65

Souris K *et al* 2016 Fast multipurpose Monte Carlo simulation for proton therapy using multi- and many-core CPU architectures *Med. Phys.* **43** 1700

Thummerer A *et al* 2020 Comparison of CBCT based synthetic CT methods suitable for proton dose calculations in adaptive proton therapy *Phys. Med. Biol.* **65** 095002

Thummerer A *et al* 2021 Clinical suitability of deep learning based synthetic CTs for adaptive proton therapy of lung cancer *Med. Phys.* **48** 7673–84

Thummerer A *et al* 2022 Deep learning-based 4D-synthetic CTs from sparse-view CBCTs for dose calculations in adaptive proton therapy *Med. Phys.* **49** 6824–39

van der Heyden B *et al* 2021 Artificial intelligence supported single detector multi-energy proton radiography system *Phys. Med. Biol.* **66** 105001

Yang M *et al* 2012 Comprehensive analysis of proton range uncertainties related to patient stopping-power-ratio estimation using the stoichiometric calibration *Phys. Med. Biol.* **57** 4095–115